5

Droplet bouncing from superhydrophobic leaf surfaces

In previous chapters, we examined droplet wettability and the rolling behavior of droplets on natural and biomimetic leaf surfaces. In this chapter, we delve into the dynamics of droplet impact, a ubiquitous interfacial phenomenon found throughout nature all around us. When a droplet impacts a solid surface, it may undergo deposition, spreading, bouncing, or splashing. We investigated surfaces with diverse wettability characteristics and physical attributes, including hydrophobic and superhydrophobic surfaces, variations in adhesion (low and high), and structures at both the micro and nano scales.

5.1 Introduction

In this chapter, we carried out investigation of the droplet impact on hydrophobic and superhydrophobic leaf surfaces with low and high adhesion features. For self-cleaning, two main mechanisms are essential: (1) droplet rolling on inclined surfaces, and (2) droplet bouncing upon impact with the surface [46]. The rolling mechanism is a well-documented phenomenon in self-cleaning and has been extensively studied for over a century, particularly regarding the morphological evolution of droplets rolling across different surface types [11, 45, 46, 205]. However, the bouncing mechanism offers intriguing new avenues for exploration, attracting increasing research interest [50]. The droplet impact reflects as a self-cleaning surface, which is related to the dynamic wetting aspect of solid surfaces. The phenomenon of droplet bouncing and self-cleaning capabilities exhibited by both smooth and textured solid surfaces is increasingly recognised for its technological importance. Nature serves as a great artist and source of inspiration. High impact of water droplet on solid surfaces is

often observed during rainfall in nature. Some plants become wet while others are non-wettable due to the inherent surface engineering prowess of nature, especially evident on superhydrophobic leaves such as lotus leaf, taro leaf, silver ragwort, etc. [82, 88, 206]. The micro- and nanotextured design of leaf surfaces has received a great deal of attention due to its multifunctional features like, adhesion, drag reduction, self-cleaning, anti-icing, and antibiofouling, etc. [11, 207–210]. However, the dewetting phenomenon of specific plant leaf surfaces is of great importance, especially in dynamic scenarios of impacting droplet. The major forces that can affect the droplet impact become important to ensure the droplet dewetting or bouncing on solid surfaces, such as interfacial tension, inertial force, viscous force, and gravity, etc. [50, 129].

When a droplet impacts a hydrophobic solid surface at high velocity, it typically progresses through three main phases: (i) a swift spreading to reach its maximum diameter on the surface, (ii) a retraction phase following this spread, and (iii) a direct rebound from the surface [50]. The time required for maximum spreading and retraction, as well as the likelihood of droplet fragmentation and the formation of satellite droplets, are significantly affected by their surface properties [50, 53, 211, 212]. In essence, the dynamics of liquid droplet impact can be analysed through the numerous dimensionless parameters [50]. However, for variable droplet kinetic energy, the Weber number (We), becomes important which scales the significance of inertia forces to surface tension forces, $We = (\rho_w u_i^2 r_\circ)/\gamma_{LA}$, where ρ_w, u_i, $r_\circ$, and γ_{LA} are the water droplet density, impact velocity, droplet radius before impacting, and surface tension, respectively. The energy loss of impacting droplet is significant for the rebounding features of the droplet, and quantified by the restitution coefficient, $e = u_r/u_i$, where u_r and u_i are the reflected and impacting droplet velocities to the surface [130]. Several studies have documented the necessary conditions for droplets to impact and rebound. The micro/nano -textured (super)hydrophobic surface invokes essential for droplet rebounding [50, 212–215]. Nevertheless, contact angle hysteresis (CAH) highly affects droplet rebounding [216, 217].

The current study aims to examine the unique topographical features as well as droplet bouncing response of four newly identified plant leaf surfaces. Two superhydrophobic with low and high adhesion characteristics and two hydrophobic features, namely *Kalanchoe fedtschenkoi*, *Ziziphus mauritiana* (Indian jujube), *Mesua ferrea* (Cobra saffron), and *Litchi chinensis* (Lychee), see Fig. 5.1. Experiments were conducted to examine droplet impact on these natural leaf surfaces, focusing on how surface structure, adhesion, and surface inclination might influence droplet spreading, contact duration, and effective rebound behavior. A mathematical model was also developed to elucidate the relationship between surface structure, impact velocity, and rebound dynamics for micro-structured hairy leaf surface.

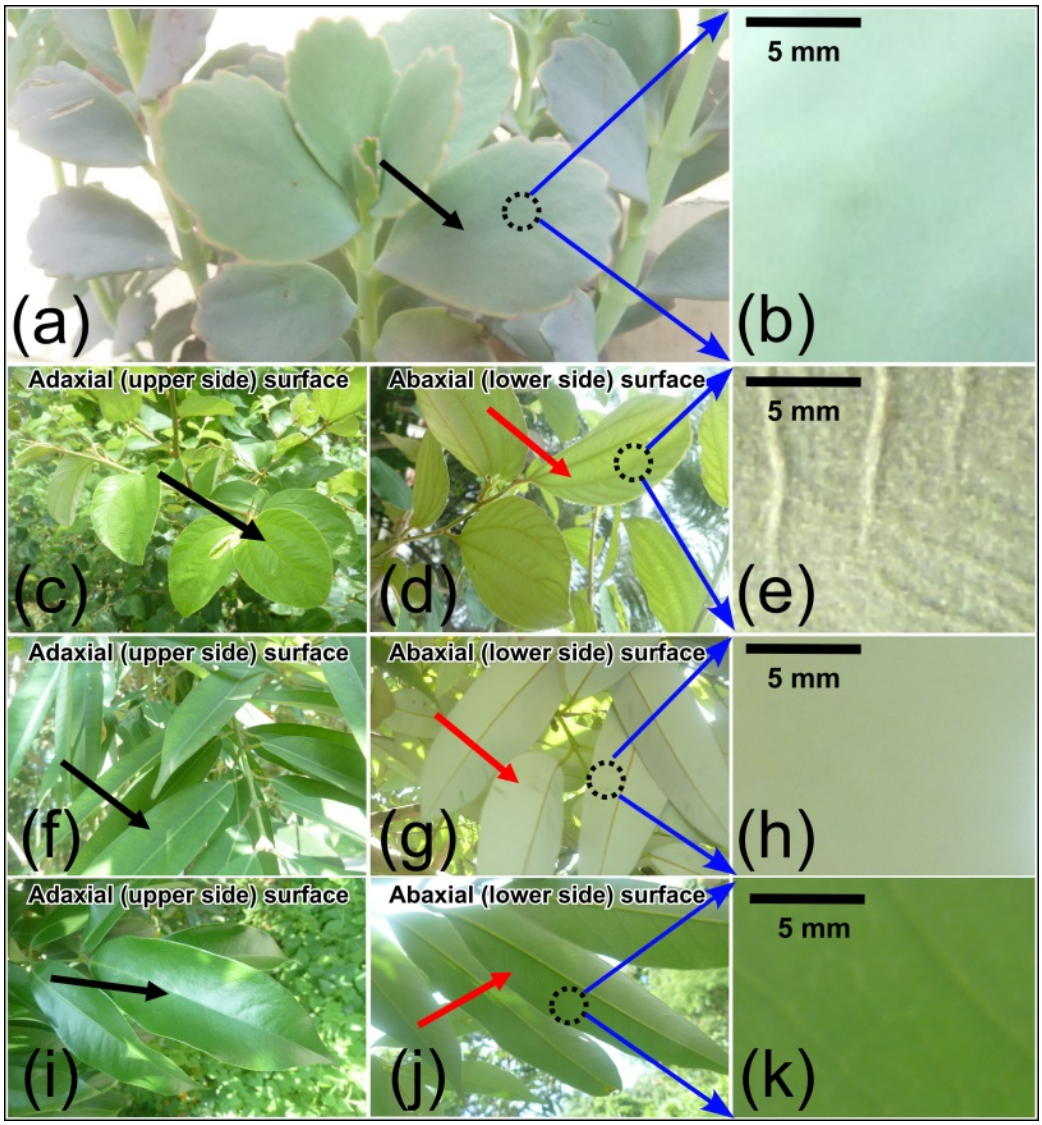

Figure 5.1: The optical photograph of tree (plant) branch with leaves. (a, b) *Kalanchoe*. (c-e) *Ziziphus*. (f-h) *Mesua*. (i-k) *Litchi*. The black and red arrows indicate adaxial and abaxial sides of the leaf surfaces.

5.2 Experimental section

5.2.1 Sample, preparation, and techniques of characterization

Fully grown healthy leaves from four plants namely, *Kalanchoe fedtschenkoi*, *Ziziphus mauritiana*, *Mesua ferrea*, and *Litchi chinensis* respectively, were collected and digital spap shown (Fig. 5.1). The fresh *Ziziphus*, *Mesua*, and *Litchi* leaves were gently collected from the decade old trees available in our university campus in the wee hour of morning. However, the *Kalanchoe* leaves collected from nearby village garden. To retain the physiological state, which might affect the surface texture, only a minimal time lag was considered between plucking of leaves and droplet character-

ization on the leaf surfaces. However, it is well known fact that the turgor pressure in cells is crucial for maintaining the structural integrity of leaf surface and depends on mechanical rigidity, cut lengths, and folding angle of leaf. In our case leaf surfaces are stable for several days. The samples were placed in a glass petri dish (If needed, place them in a highly humid chamber to preserve the structural integrity and smooth surface of the leaves) carefully in ambient environment and air blown to remove away any contaminant particles like mist, dust, pollen, etc. from the leaf surfaces. The surface morphologies of the leaves were captured using a scanning electron microscope (SEM, *Zeiss Σigma VP*). For SEM characterization, the sample was cut into segments of size ∼0.5 × 0.5 cm^2 sections and then, platinum was sputtered on them to create conductive coating (∼7 nm) on leaf surfaces. To prevent the collapse of nano- and microtexture due to water evaporation from the leaf surfaces under the high-vacuum conditions during conductive platinum coating (several nanometres thick) and imaging, leaf dehydration was required. Infact, the dehydration of biological tissues, presents specific challenges. Various dehydration methods are available, including air drying, critical-point drying (CPD), chemical fixation, and freeze-drying [218]. However, different plant leaves have varying cell strengths and structures, requiring distinct drying techniques [219]. In our study, a simple air-drying method at room temperature was chosen for all four leaves. The collapse of cells, leading to morphological changes, occurred due to the sudden change in turgor pressure inside the cells. To mitigate this, the leaves were cut into larger sections and dried slowly. However, the reduction in turgor pressure during dehydration (water loss) is influenced by factors such as mechanical rigidity, leaf cut lengths, and folding angles [220]. This complex process can differ between plants due to variations in the composition of their cell walls, including cellulose, hemicellulose, lignin, and other components [221].

5.2.2 Droplet wettability and droplet impact experiments

The static and dynamic water contact angle (WCA) characterization of leaf surfaces was conducted considering at least three specimens from each leaf-type choosing. The specimens were carefully cut into 2 × 2 cm^2 pieces as needed, typically from the mid-region of the leaf surfaces. These pieces were affixed onto microscope glass slides using double-sided adhesive tape and mounted on an advanced contact angle meter setup (*Kyowa Interface Science®*, Japan) in our laboratory. For all experiments, deionized water droplets are taken with a volume of ∼5 μL. In the WCA measurement setup, micro-droplets were generated using a syringe pump connected to the contact angle meter and gently placed on the specimen. The CAs were determined by analyzing images captured on a high-speed camera (60 *fps*) under white light illumination.

For CHA and roll-off angle were determined by identifying the tilting angle (T.A.) at which a droplet begins to roll down. To perform the measurement, the specimen stage was tilted vertically over a range from ∼0° – 90°. The droplet bounding experiments were conducted on ∼2 × 2 cm^2 leaf's pieces affixed onto microscope glass slides as discussed. The impacting droplet volume was kept ∼5 μL (diameter ∼2.12 mm) which is created at the tip of the needle connected to controlled microfluidic pump system. Fig. 5.2 illustrate the droplet bouncing experimental setup. The droplet impact velocity, u_i (or *We*) was varied by changing height of needle tip by changing needle holder position over scaled vertical stand. In this study, we considered three distinct impacting heights: ∼5 mm, 25 mm, and 45 mm and correspondingly, *We* ∼2.8, 14.4, and 25.8, respectively. The droplet impact on leaf surfaces were captured using a high-speed camera (*Phantom LAB3a10, Micro® LAB*) offering high resolution (1280 × 1024 pixels) and requisite frames per second (∼2000 *fps*). For angle-dependent droplet impact on a leaf specimen, a platform with an adjustable tilting angle was positioned on the substrate stage. The camera, leaf substrate, needle tip, and white light source were aligned along the same optical axis, as shown in Fig. 5.2. The recorded videos were analysed using Python code, while the extracted images were processed with *ImageJ* software.
All the experiments were carried out at room temperature (∼ 25 ± 1° C) and atmospheric pressure.

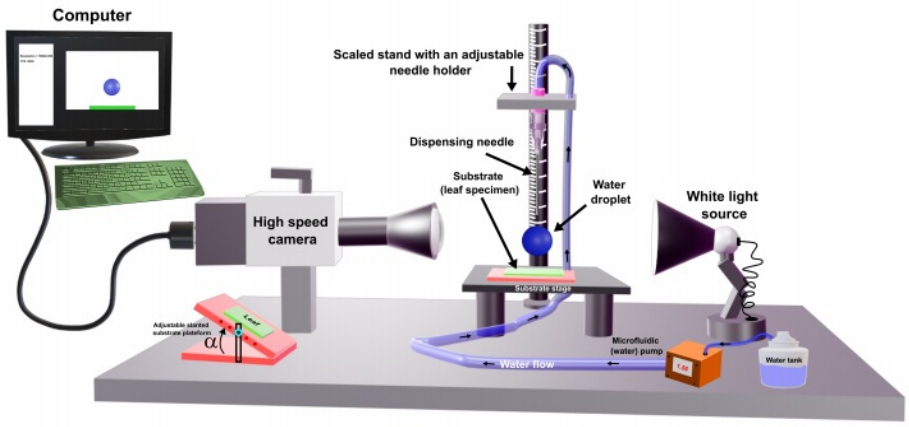

Figure 5.2: Schematic illustrates the droplet bouncing experimental setup.

5.3 Surface morphology of leaf specimens

The *Kalanchoe*, *Ziziphus*, *Mesua*, and *Litchi* leaves shown distinct micro-nano structures. The surface morphologies with different magnifications were captured using SEM imaging. The completely air -dried leaf specimens of four different plants mi-

croscopic images can be found in Fig. 5.3. It should be noted here, the *Kalanchoe* leaf surfaces possess equi-facial appearance and surface structural features, and therefore only adaxial (upper side) leaf surface was considered in the current work. However, other three plant (*Ziziphus*, *Mesua*, and *Litchi*) leaf surfaces shown different adaxial (upper side) and abaxial (back side) surface structures. As for experiment, the abaxial side of *Ziziphus*, *Mesua*, and *Litchi* leaf surfaces have been selected due to specific surface morphology compared to their adaxial counterpart.

Kalanchoe fedtschenkoi prefer to grow in partial dry and low intense light places. It is succulent indoor house/garden plant and belongs from *Crassulaceae* family. The leaves of *Kalanchoe* plant are thick and stores water that makes capable to thrives in low water (rainfall) region. The leaves are partially white and green colour with obovate shaped and crenate edges. The crenate edges turn in to partial red under strong sunlight. The size (length $\times$ width) of the leaf's $\sim$4.5 $\times$ 3.5 cm^2 with thickness $\sim$1–1.5 mm. Micromorphological features of the *Kalanchoe* adaxial surface are clearly visible in the optical and SEM images at various magnifications, as shown in Figs. 5.3($a_1 - a_3$). The surface consists of a single-level nanostructure of waxy, curved chip-shaped features, arranged in groups resembling clusters spread across the leaf surface.

Ziziphus mauritiana is a fruit bearing plant from the *Rhamnaceae* family. This plant is found in a variety of sizes and features thorny shrubs. It can survive in extreme temperature ranges. The leaves are oval or elliptic in shape with smooth edges, and their size ranges $\sim$4.7 $\times$ 2.5 cm^2 – 9.6 $\times$ 7.3 cm^2. The adaxial side appears dark green, while the abaxial side is partially white with green. It can be observed in Fig. 5.3($b_1 - b_3$), the abaxial side of tender state leaf surface exhibits a hairy (fibrous), matted, single-level structure with fiber's average diameter $\sim$7.1 μm. These hairs are typically hydrophobic trichomes, which may be unicellular, multicellular, or branched, protruding from the epidermal tissues and distributed in a nonwoven pattern across the abaxial leaf surface.

Mesua ferrea plant found in tropical wet climate belong from *Calophyllaceae* family. The tender leaves initially display a mixture of red and semi-transparent green, gradually changing to dark green as they mature. The leaves are liner in shape with smooth edges, and their size $\sim$14.5 $\times$ 4.5 cm^2. The adaxial (upper) surface of the leaf appears dark green, while the abaxial side is white. As shown in Fig. 5.3($c_1 - c_3$), the abaxial surface of the mature leaf exhibits densely packed micro-bumps, which appear fractal like waxy nano-structure covering the surface.

Litchi is a fruit-bearing plant from the *Sapindaceae* family. Its leaves have a lanceolate shape with smooth edges, featuring a dark green adaxial side and a whitish-green abaxial side. The lanceolate-shaped leaves have smooth edges, with sizes $\sim$13 $\times$ 4 cm^2. The abaxial leaf surface as shown in Figs. 5.3($d_1 - d_3$), is highly packed with

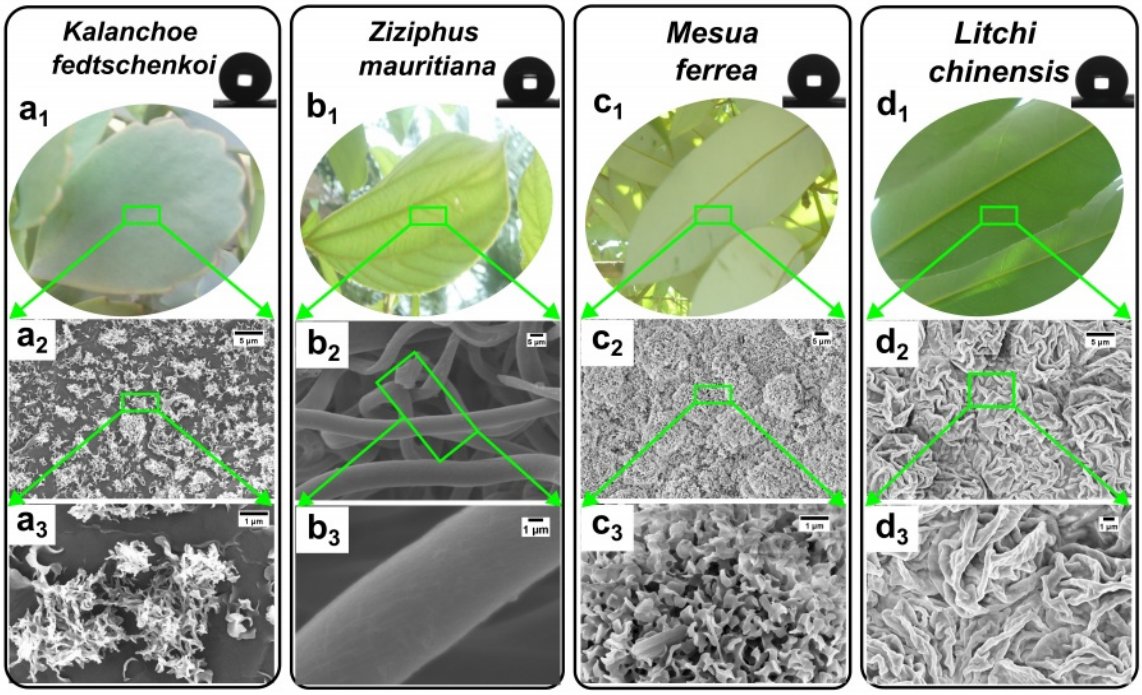

Figure 5.3: (a_1, b_1, c_1, d_1) The digital photograph of four distinct plant leaves (adaxial, abaxial). SEM imaging with different magnifications (scales: 5μm, 1μm) of four distinct plant species. (a_2, a_3) *Kalanchoe*, (b_2, b_3) *Ziziphus*, (c_2, c_3) *Mesua*, and (d_2, d_3) *Litchi* leaf textures. Note the zoomed in images from top to bottom in each column. To be specific, hairy matted micro-fiber structures can be viewed for *Ziziphus* species (see Appendix III, (Fig. A.12)).

waxy micro-nano hierarchical structure, cuticular folds (see Appendix III, table T.4).

5.4 Wettability, droplet impact, and shape analysis

5.4.1 Contact angle (CA), hysteresis (CAH) and roll-off

The static water contact angle (WCA), and contact angle hysteresis (CAH) were measured using contact angle meter of four specific plant leaf specimens namely, *Kalanchoe*, *Ziziphus*, *Mesua*, and *Litchi*. These plant leaves were considered based on high WCA and adhesion (high and low) aspects in the current study. The adhesion properties of leaves were quantified by measuring CAH $(\theta_a - \theta_r)$ using tilting plate method. The plot of WCA and CAH of *Kalanchoe*, *Ziziphus*, *Mesua*, and *Litchi* leaf surfaces are depicted in Fig. 5.4. Observably, the *Kalanchoe* and *Ziziphus* (tender state) leaf surface exhibit superhydrophobicity with WCAs as high as, $\sim$156° and $\sim$151°; respectively. However, the *Kalanchoe* leaf shown low CAH of $\sim$4° with very low adhesion. The droplet roll -off at very small T.A. of $\sim$3°. The abaxial side *Ziziphus* leaf surface gave a high CAH of $\sim$30° with roll -off angle $\sim$21°. The other two, *Mesua* and *Litchi* leaf surfaces shown WCA in hydrophobic region with respective

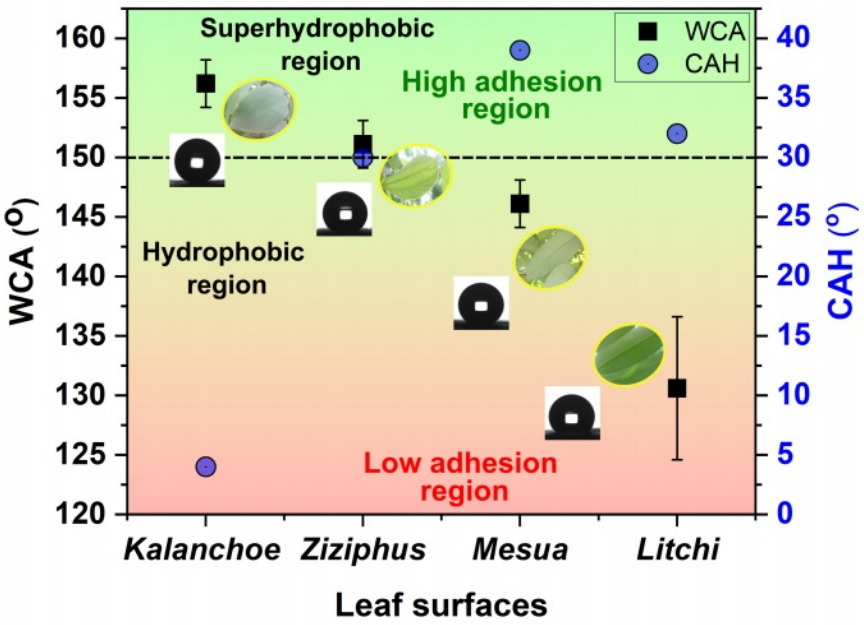

Figure 5.4: The plot of WCAs and CAHs for *Kalanchoe*, *Ziziphus*, *Mesua*, and *Litchi* leaf surfaces. The horizontal dashed line separates hydrophobic and superhydrophobic regions, whereas pink and green areas mark low- and high-adhesion regimes; respectively.

values ∼146° and ∼130° with CAH ∼39° and ∼32°. Furthermore, the *Mesua* and *Litchi* leaf surfaces possess high CAH without rolling action up to T.A. ∼ 90°.

Interestingly, *Kalanchoe* and *Ziziphus* leaf surfaces exhibit superhydrophobicity but with low and high adhesion characteristics, respectively. As discussed, *Kalanchoe* leaf have nanoscale surface morphology whereas the abaxial *Ziziphus* leaf comprises hairy matted single level microscale surface structure. Both surfaces possess superhydrophobicity attributable to porous surface with distinct scale-levels and structures. Essentially, the porosity of structured surfaces creates air pockets, which facilitate a low-wetting regime. In other words, the trapped air reduces the solid-liquid (water) contact area, resulting in a suspended wetting state on the leaf surface. Also, *Mesua* and *Litchi* leaf surfaces exhibit a densely packed waxy structure, leading to minimal porosity. This results in low WCAs combined with high adhesion.

5.4.2 Complete and partial rebound state

The droplet bouncing experiment is carried out after having characterizing WCA and adhesion properties of the four selected natural leaf specimens. The two superhydrophobic leaf specimens, *Kalanchoe* with low adhesion and the *Ziziphus* with high adhesion, as well as the two hydrophobic leaf specimens (*Mesua* and *Litchi*) with high adhesion, differ in scale level and surface morphology. As discussed in experimental section, the water droplet considered was of small volume, ∼5 μL. The

static droplet forms uniform cap shape on a solid surface by balancing the capillary adhesion force, droplet weight, and Laplace pressure. There are two limiting cases where the droplet volume, V, can choosen to see the effects droplet impact effect on solids. When the droplet size is larger than the capillary length, $r_o > l_c = \sqrt{\gamma_{LA}/\rho_w g}$, where g is the gravitational acceleration, droplet's weight dominates over the capillary adhesion force, and the droplet shape become non spherical [222]. However, for $r_o < l_c$, capillary force will become effective. The droplet shape is able to retain spherical under gravitational effect. In this experiment, we have considered small droplet size of radius ($r_\circ$) ~1.06 mm. For given DI water droplet, ρ_w ~998 kg/m^3, γ_{LA} ~72 mN/m, g ~9.8 m/s^2, l_c ~2.7 mm [223]. Usually, when a water droplet impacts a (super)hydrophobic surface, it typically spreads uniformly in all directions in a pancake-like configuration without retracting, until its kinetic energy approaches zero. At this point, the droplet reaches maximum contact with the solid surface, achieving its maximum spreading diameter. However, during droplet spreading, the converted kinetic energy into surface energy, causing the droplet to retract and eventually fully rebound. Without affecting water droplet viscosity and standard environmental conditions, the droplet impacting, spreading, and rebounding process, to a great extent, depends on nature of solid surface. The impacting scenarios of droplet of diameter, $D_\circ$ ~2.12 mm on leaf surfaces with zero tilting angle for different *We* numbers are depicted in Fig. 5.5. At low *We* (~2.8) value, the droplet spread and rapidly retracted. After retraction, the droplet fully rebound without leaving any secondary droplets on the leaf specimen for low and high adhesion superhydrophobic and hydrophobic (high adhesion) leaf surfaces, as shown in Fig. 5.5(a).

As droplet impacting height increases for, *We* ~14.4, the maximum spreading reached and the corresponding maximum diameter (D_{max}) tending to increase for all the leaf surfaces. After reaching D_{max}, the droplet retracted and fully rebound as for *We* ~2.8 in case of low adhesion superhydrophobic *Kalanchoe*, adhesion superhydrophobic *Ziziphus* and hydrophobic *Mesua*, *Litchi* leaf surfaces. However, for higher *We* ~14.4, the high adhesion superhydrophobic *Ziziphus* leaf surface exhibits droplet breakup during detachment, as shown in Fig. 5.5(b). The impacting droplet is fragmented into a fully rebounding 'parent droplet' and a 'residue droplet' that remained attached to the surface as indicated by red dotted circle and square, shown in Fig. 5.5(b). The residue droplet's volume was smaller than that of the parent droplet ((see Appendix III, (Fig. A.13)). The partial rebounding of the droplet on hairy matted *Ziziphus* leaf surface invoked a wetting transition from the suspended state to the partial collapsed state, as depicted in Fig. 5.6. The *Ziziphus* leaf surface arises micro-scale hairs of irregular, nonwoven pattern with high porous matted structure. Large size air voids beneath the wetted area may fail to maintain the Laplace pressure balance between the trapped air in the voids and the water droplet inter-

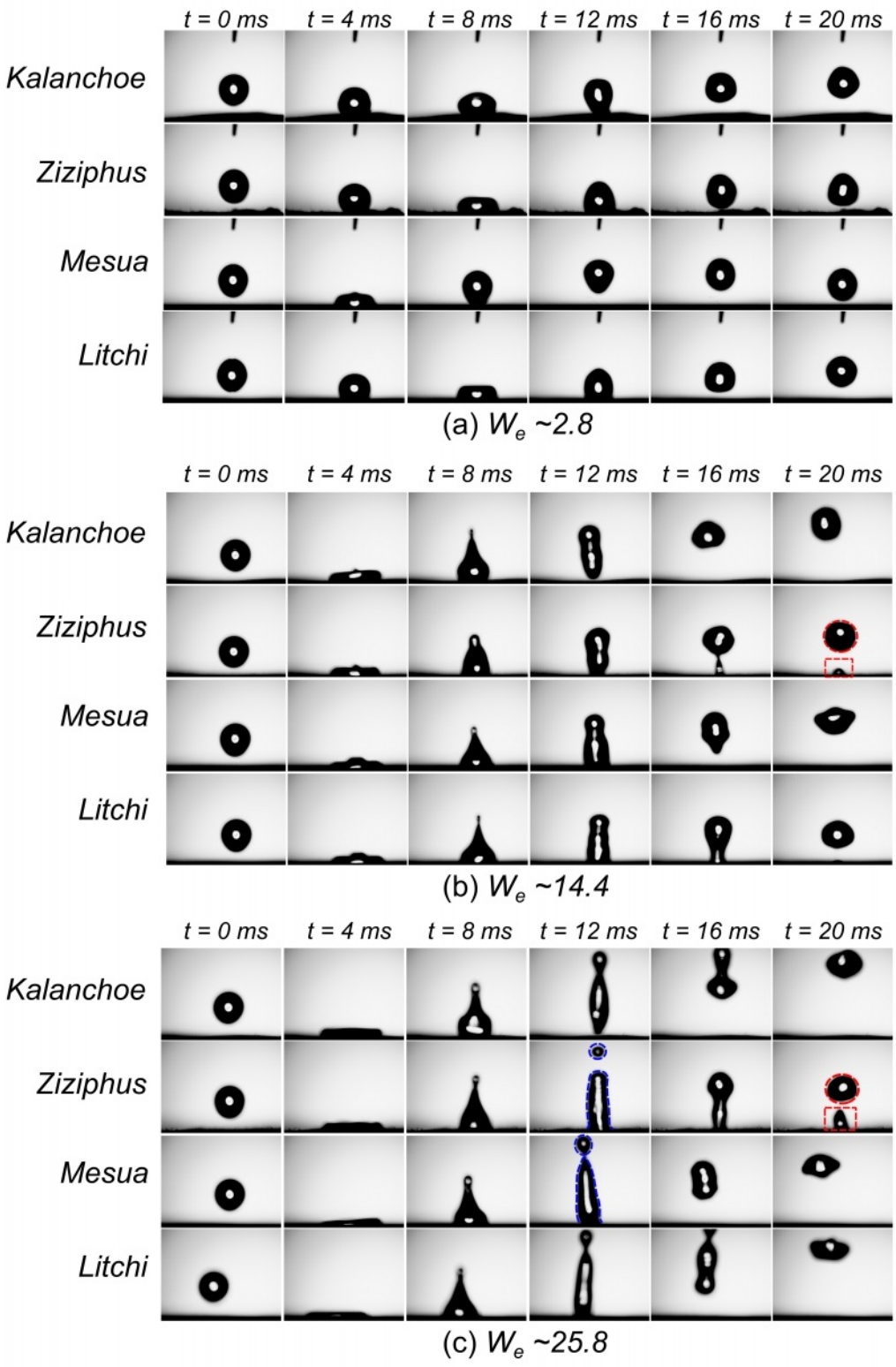

Figure 5.5: The optical snapshots (at t = 0–20 ms) acquired from high-speed imaging capture the water microdroplet (D_o) impact process on (super)hydrophobic leaf surfaces at different Weber numbers: (a) $We \sim 2.8$, (b) $We \sim 14.4$, and (c) $We \sim 25.8$. Note the impact, spreading, retraction, and partial/complete rebound characteristics, as applicable to each specimen type. For higher We, partial rebound with fragmented entities is clearly visible for the *Ziziphus* species.

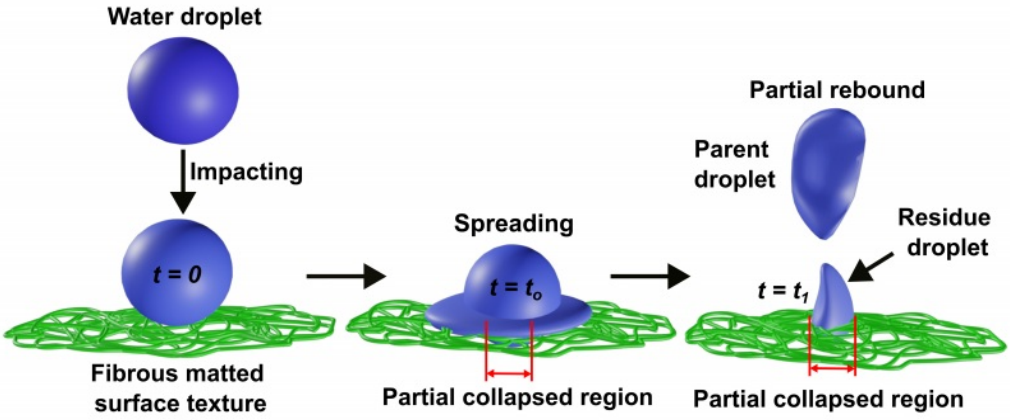

Figure 5.6: The schematic represents the droplet wetting transition during impact process on hairy matted (*Ziziphus* leaf) surface structure. The arrows represent stages involved from droplet impact to partial rebounding event.

face. This imbalance, combined with the dynamic impact pressure, results partial water insertion, leading to a wetting transition from the Cassie state to the Wenzel (collapsed) state. In the same way, as for *We* ∼25.8, the droplet breakup occurred for *Ziziphus* leaf surface with slightly higher residue droplet volume, as shown by the red dotted circle and square in Fig. 5.5(c). Furthermore, jet formation was observed during droplet rebound at *We* ∼14.4 and ∼25.8 across all leaf surfaces as can be seen for $t = 8$ ms, Figs. 5.5(b) and 5.5(c) (see Appendix III, (Fig. A.14). However, significant neck evolution occurred only in the latter case. In addition to droplet breakup on the surface, a breakup occurred near the jet neck for *We* ∼25.8, producing a tiny satellite droplet for *Ziziphus* and *Mesua* leaf surfaces, depicted with dotted blue circle in Fig. 5.5(c) (see Appendix III, (Fig. A.15). For the *Kalanchoe* and *Litchi* leaf surfaces, while the droplet breakup appeared likely near the jet neck, it did not occur, as it needed slightly higher impacting velocity (*We* >25.8). The droplet was fragmented with ∼64% parent droplet of initial impacting droplet volume (∼5 μL) for *We* ∼14.4 in case of *Ziziphus* leaf surface. However, for Weber number (*We* ∼ 25.8), a decrease in parent droplet volume (∼48.8%) and increase in residue volume was observed. Additionally, a satellite droplet of ∼ 3.5% of the initial volume was observed. Similarly, as for *We* ∼25.8, *Mesua* shown jet breakup near neck with satellite drop ∼8.7% of the initial volume. At $t = 12\pm1$ ms, the rebounding droplet experienceson maximum vertical stretched height alike jet for all leaf surfaces. The dimple shape jet observed in low adhesion *Kalanchoe* leaf surface however, the cylindrical alike shape, more prompt in *Ziziphus*, found for high adhesion leaf surfaces, are indicated by blue dotted line in Fig. 5.5(c).

5.4.3 Cassie to Wenzel wetting transition criterion

When a droplet impacts a superhydrophobic surface at a specific velocity, it can undergo a complete rebound, bouncing off the surface. However, the outcome of the impact, such as a wetting transition, depends on the surface structure and the droplet's kinetic energy [53, 224, 225]. In our experiments, partial rebound phase was observed exclusively on hairy matted structures. Here, we examine the impact of a water droplet on a superhydrophobic hairy matted surface. When the droplet size is smaller than the capillary length, l_c, the influence of gravity on the droplet shape becomes negligible [222]. For water, this occurs when the droplet radius $r_\circ$ is less than l_c ~2.7 mm. Under these conditions, the hydrostatic pressure exerted by the droplet, ρgh, on the hairy surface can be ignored [226]. Consider a hairy matted structure consisting a regular array of hydrophobic hairs (fibers) with average radius r, and separation d as shown in Fig. 5.7. $\angle OBB' = \angle DBC - \left(\frac{\pi}{2} - \angle A'BC\right) - \angle OBD$. Since, $\angle A'BC = \angle A'BA + \angle ABC = \frac{\pi}{2} - \varphi + \pi - \theta_a$, $\angle OBD = \theta_a - \frac{\pi}{2}$. Therefore, $\phi = \theta_a - \left(\frac{\pi}{2} - \frac{\pi}{2} + \varphi - \pi + \theta_a\right) - \theta_a + \frac{\pi}{2} = \frac{3\pi}{2} - \varphi - \theta_a$. As shown in Fig. 5.7, the Cassie liquid -solid fraction is given by, $f = \frac{EB}{B''B'} = \frac{r\varphi}{r+d}$. Therefore, $O'O'' = \frac{2r\varphi}{f}$, and $BB' = OB\cos\phi = R_c\cos\left(\frac{3\pi}{2} - \varphi - \theta_a\right)$, $O'O'' = 2(B''B + BB') = 2\left(r\sin\varphi + R_c\cos\left(\frac{3\pi}{2} - \varphi - \theta_a\right)\right)$. The radius of curvature of water bridge given as,

$$R_c = \frac{\sin\varphi - \frac{\varphi}{f}}{\sin(\varphi + \theta_a)}\, r. \tag{5.1}$$

Using Eq. (5.1), the Laplace pressure due to water bridge curvature at liquid -air interface is given by;

$$\Delta P_L = \frac{2\gamma_{LA}}{R_c} = \frac{2\gamma_{LA}\sin(\varphi + \theta_a)}{r\sin(\varphi) - (\frac{\varphi}{f})}. \tag{5.2}$$

From Eq. (5.1), as φ increases, the curvature of the bridge shifts downward, making contact with the smooth substrate, which results in an increase in the wetted area. In the case of static equilibrium, when $\Delta P_L = 0$, the curvature flattens. According to Eq. (5.1), to shift the curvature and increase the spreading parameter, an applied pressure is necessary. Suppose a droplet impacts a hairy matted surface with an initial velocity u_i. The dynamic pressure exerted by the droplet is given by [225, 226]:

$$P_d = \frac{1}{2}\rho_w u_i^2. \tag{5.3}$$

Using Eqs. (5.2) and (5.3), the critical impact velocity of a droplet, at which the transition from the suspended to the collapsed state occurs, can be determined. Complete rebound happens when the dynamic pressure is less than the Laplace pressure. How-

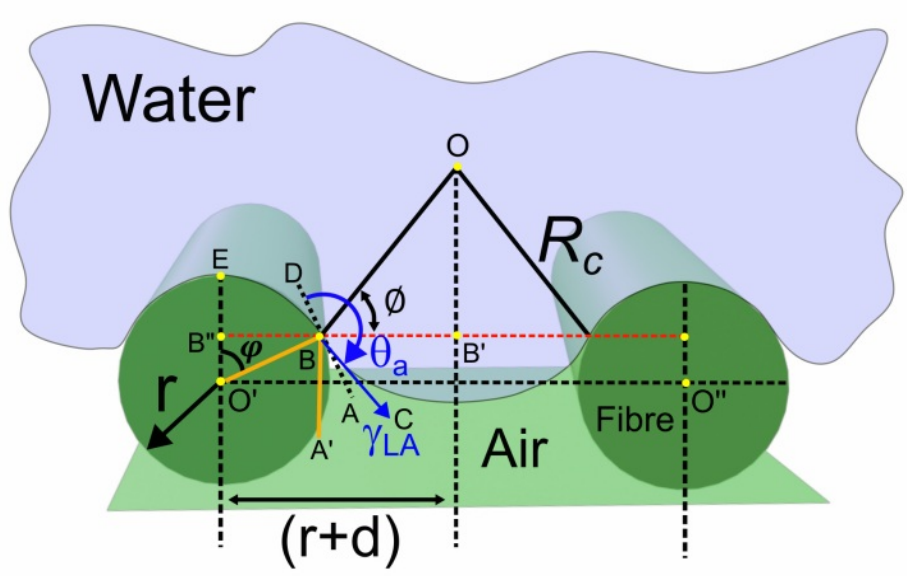

Figure 5.7: Schematic illustrating the dynamic water bridge formation during droplet impact between two hydrophobic fibers (hairs) of radius r, with an average separation between microfibers of $2d$. The trapped air beneath the water exerts an upward pressure, causing the water to form a curvature of radius R_c, which results in a Laplace pressure.

ever, the transition from the Cassie to the Wenzel state takes place when the dynamic pressure exceeds the Laplace pressure, as defined by the following condition:

$$u_i > \sqrt{\frac{((4\gamma_{LA}\sin(\varphi+\theta_a)}{\rho_w r\sin(\varphi)-(\frac{\varphi}{f})}}. \tag{5.4}$$

Equation (5.4) illustrates the correlation between the wetting transition and impact velocity, specifically for velocities exceeding a critical threshold, as shown in Fig. 5.6. For $u_i \sim 31$ cm/s ($We \sim 2.8$), no partial rebound is observed on *Ziziphus* leaf surface, depicted in Fig. 5.5(a). However, as the Weber number increases, partial rebound occurs at $u_i \sim 70$ cm/s ($We \sim 14.4$), shown in Figs. 5.5(b) and 5.5(c). Therefore, the critical impact velocity must lie above $u_i \sim 31$ cm/s.

5.4.4 Effect of surface inclination

The impact process of droplets can be influenced by various key parameters. However, upon closer observation in nature, it is evident that plant leaves, inclined relative to branches and leaves, cause rain droplets to impact at an angle. This has inspired us to investigate droplet impact on inclined leaf surfaces. We considered three different tilting angles of the leaf surfaces, ∼10°, 20°, and 30° for a given Weber number (We ∼25.8). The high-speed snapshots of droplet impact on inclined leaf surfaces are shown in Fig. 5.8.

For a given Weber number, the impact dynamics of a droplet ($D_\circ$ ∼2.12 mm) on

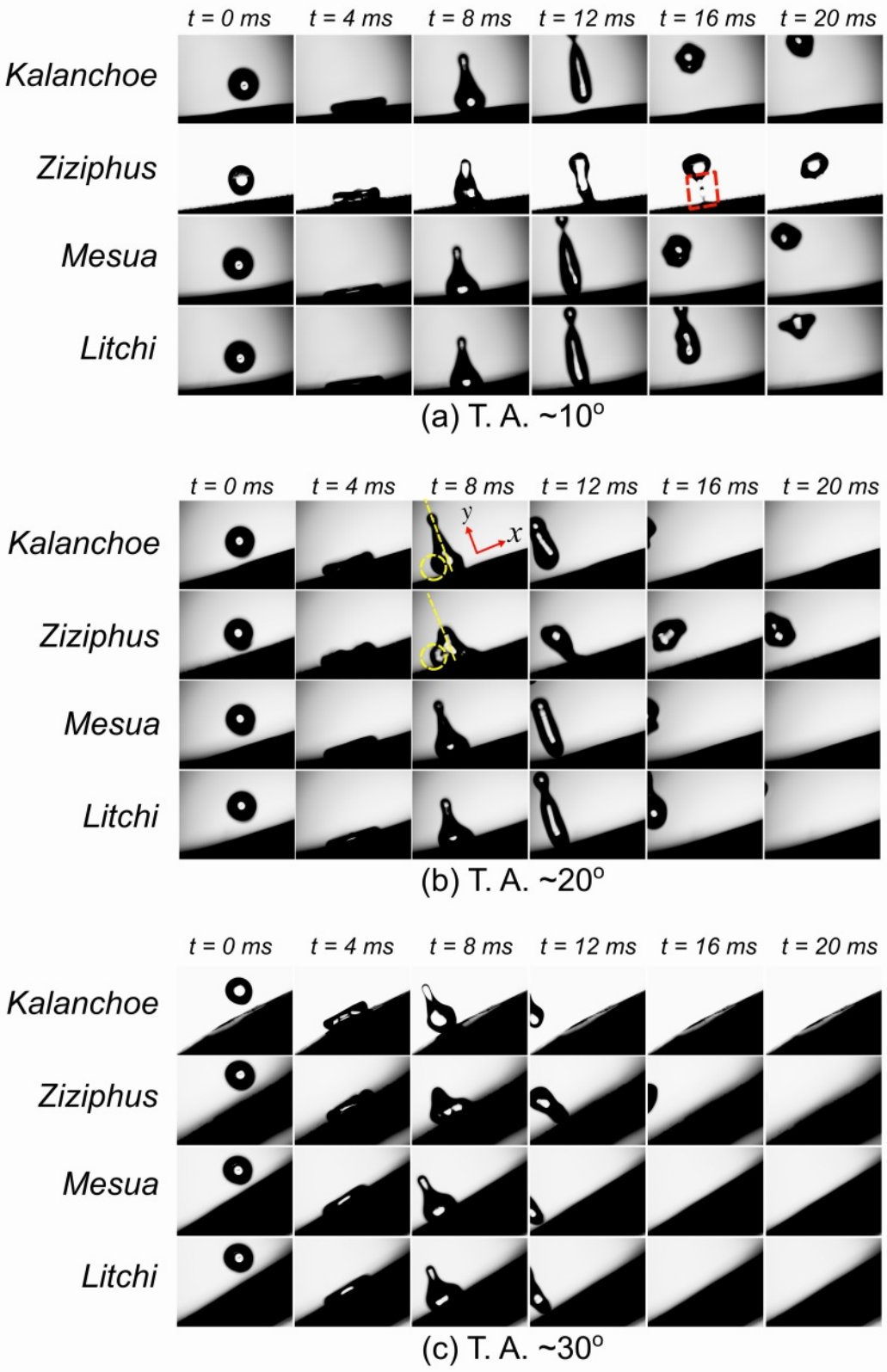

Figure 5.8: The high-speed captured images of water droplet (*Do*) impact process on (super)hydrophobic leaf surfaces at different surface inclinations (*We* ~25.8, t = 0–20 ms): (a) T.A. ~10°, (b) T.A. ~20°, and (c) T.A. ~30°. Note the tilted surface offering spreading and rebound characteristics with jet and bottleneck features.

inclined leaf surfaces differ from those on a horizontal surface. When a droplet come in contact on an inclined surface, the normal (y-direction, $u_y = u_i cos\theta$) and tangential (x-direction, $u_x = u_i sin\theta$) velocity components compete, leading to asymmetric spreading and retraction, (Fig. 5.8). This causes rapid detachment of droplet from the surfaces, (Fig. 5.7 and Fig. 5.8), $t = 12$ ms. As the surface inclination increases, the droplet detachment would expedite for all the leaf specimens. However, the detachment on low-adhesion superhydrophobic *Kalanchoe* leaf surface occurs more promptly compared to hydrophobic surfaces. On high-adhesion superhydrophobic *Ziziphus* leaf surface, partial rebounding occurs at small inclination angles (∼10°), Fig. 5.8(a). However, with further increase in inclination, a complete rebound state is achieved, without any evidence of a wetting transition, Figs. 5.8(b) and 5.8(c). Furthermore, the *Ziziphus* leaf surface offers a slow detachment as compared to other three leaf surfaces due to high adhesion characteristics. The droplet initially spreads asymmetrically, flattening like a pancake. However, during retraction, the droplet base expands tangentially, causing an asymmetrical rebound with jet-like shape, $t =$ 8-16 ms, (Figs. 5.8(a-c)).

5.4.5 Droplet rebounding trajectory

The rebounding trajectory of droplets is a fascinating exploration of fluid dynamics, characterized by intricate interactions influenced by various physical parameters, including droplet size, viscosity, impact height, surface tension, and surface adhesion. The extent of rebound is determined by the coefficient of restitution, which measures the energy loss during impact; a higher value indicates a more elastic rebound. To assess how surface adhesion and wettability might influence the droplet height over time, collected data were analysed from all the leaf specimens, *Kalanchoe*, *Ziziphus*, *Mesua*, and *Litchi*. By tracing the droplet's impact on a leaf surface and observing its deformation, one can map the trajectory of both the spherical and deformed (splashing and rebounding) droplet. The periodic trajectory of a bouncing water droplet was analysed by processing captured images (videos) with Python code that utilizes the open-source computer verson library *OpenCV*. To be mentioned, droplets were released from different heights of ∼5 mm, 25 mm, and 45 mm. The analysis relies on code designed for dynamic object (droplet) detection within the camera's view area, based on captured video footage. However, for droplets released from heights of ∼25 mm and 45 mm, the initial dynamics are outside the camera's field of view. Therefore, we used the normalized height ($h/h_{\max}$) as the y-coordinate for the bouncing droplet to its maximum y-coordinate in view area. The water droplet ($D_\circ$ ∼2.12 mm) height *vs* time profile for *We* ∼2.8, 14.4, and 25.8, can be found for all leaf surfaces, shown in Fig. 5.9. The red arrows show an incoming droplet (upside)

from three different heights, designated as $h = 0$, Fig. 5.9(a). The droplet travels downward (y-direction) to the leaf surface, and upon impact, it rebounds. The green dotted circles indicate that for higher Weber numbers, the droplet moves out of the camera's view after certain numbers (n) of bounding. Regions I and II in the plots indicate that after the droplet bounces several times (I), it eventually comes to rest on the surface and oscillates (II) until it reaches a stable state. In Fig. 5.9(b), a peak is observed in region II as a result of the breakup of satellite droplets. In region I, for the *Ziziphus*, *Mesua*, and *Litchi* leaf surfaces, droplet oscillations are also present, which are caused by the time lag associated with different Weber numbers, as shown in Figs. 5.9(b-d).

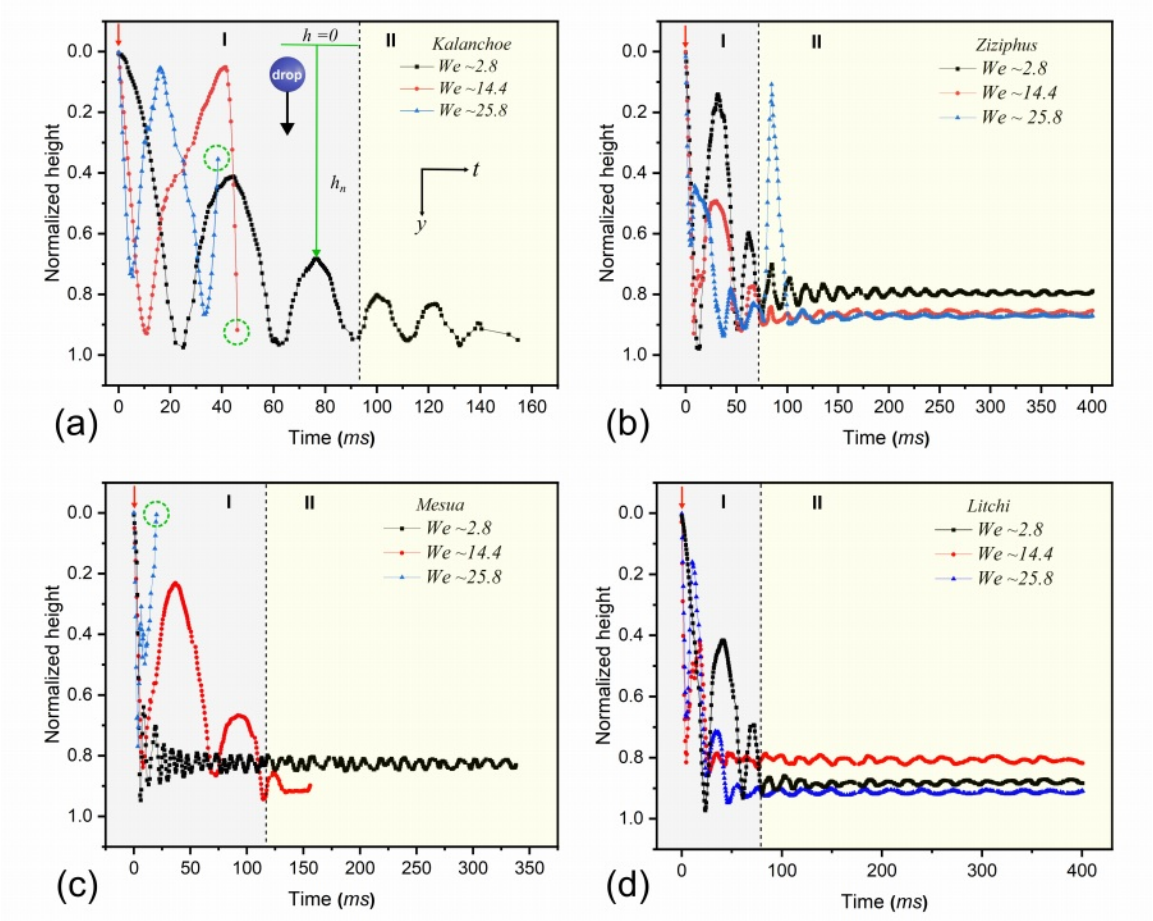

Figure 5.9: The plots depict the time-dependent bouncing profiles of droplets on leaf surfaces across various Weber numbers. (a) *Kalanchoe*, (b) *Ziziphus*, (c) *Mesua*, and (d) *Litchi*.

5.4.6 Maximum spreading and contact time (τ_c)

When a droplet impacts a solid surface, it generates dynamic pressure upon contact. The droplet counteracts this pressure using its internal Laplace pressure, which arises from surface tension. The extent of the droplet's deformation and spreading depends on the impact velocity u_i relative to the inertial-capillary speed, u_γ. Specifically,

this relationship can be quantified by the We, where $u_i = u_\gamma \sqrt{We}$. A higher Weber number indicates that the impact velocity is significantly greater than u_γ leading to greater deformation and spreading due to dominant inertial forces. Conversely, a lower Weber number suggests capillary forces are more influential, maintaining the droplet's shape. The maximum spreading diameter ($D_{\max}$) of a droplet is reached when its initial kinetic energy is fully dissipated by the end of the spreading phase. During retraction, surface energy is gradually converted back into kinetic energy, enabling the droplet to contract. However, a part of the surface energy is also expended in overcoming viscous dissipation and resisting the frictional forces at the contact line, which affect the spreading dynamics. The characteristics of droplet spreading are often described by a dimensionless maximum spreading parameter, $\beta_{\max} = D_{\max}/D_o$, which represents the extent of spreading and depends on factors, including the droplet's initial kinetic energy, surface tension, viscosity, and the surface properties it encounters. A higher spreading parameter value signifies greater spreading, which typically occurs with lower surface tension or a higher Weber number (We), representing increased impact energy. The plot of $\beta_{\max}$ against Weber numbers for all leaf specimens are shown in Fig. 5.10(a).

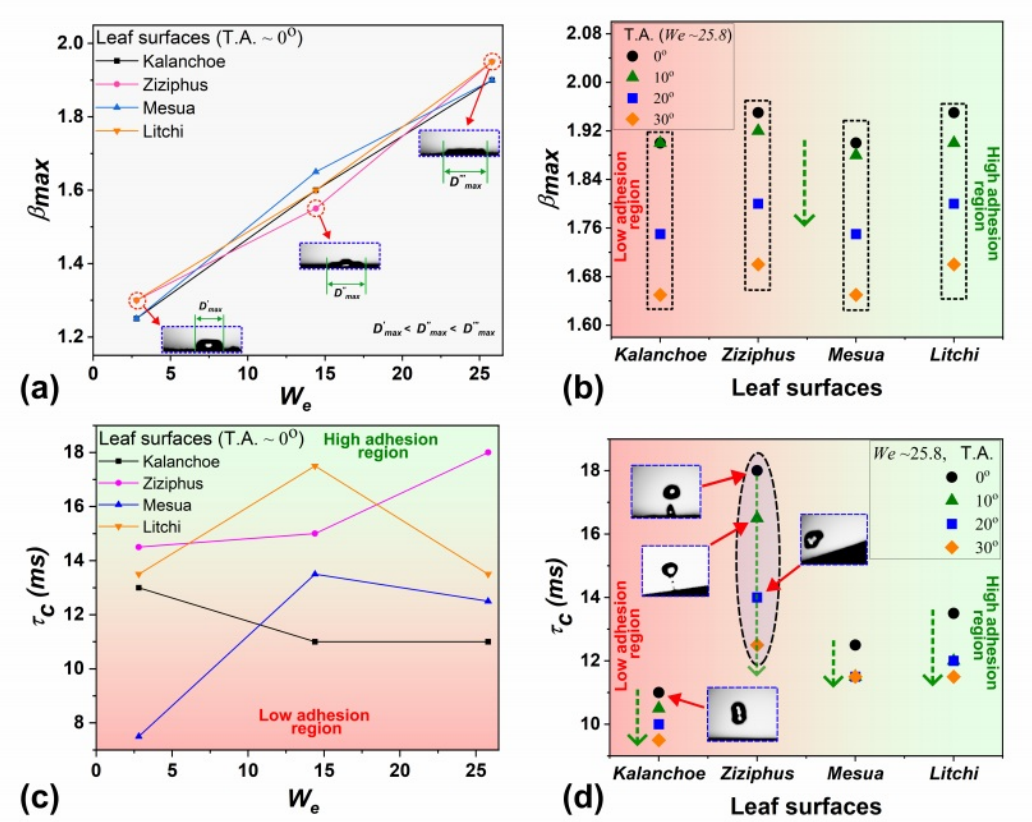

Figure 5.10: (a) and (b) display the maximum spreading profile of the droplet impact across various leaf surfaces, with changes in Weber numbers and surface tilt angle (T.A.), respectively. (c) and (d) depict the droplet contact time in relation to Weber numbers and surface inclinations; respectively. The dotted green arrow lines indicate decreasing trends.

As *We* number increases in the range of ∼2.8 -25.8, the maximum spreading parameter increases up to approximately 1.5 times to its initial spreading parameter for all leaf surfaces. However, the β_{max} decreases as the surface inclination increases for a given Weber number, *We* ∼25.8, for all leaf surfaces Fig. 5.10(b). The degree of (super)hydrophobicity and surface adhesion slightly influences on β_{max}. However, surface inclination effectively decreases the β_{max} for all leaf surfaces. During the process of maximum spreading and retraction, the duration for which the droplet remains in contact with the solid surface, known as the 'contact time', τ_c, is influenced by the droplet's inertia and capillarity (see Appendix III, (Fig. A.16). The droplet contact time for all leaf surfaces of different wetting and adhesion characteristics are depicted in Fig. 5.10(c). The parameter τ_c is slightly influenced by low and high adhesion aspect, shown in Fig. 5.10(c). However, surface inclination is much affected on τ_c for *We* ∼25.8, Fig. 5.10(d). The (super)hydrophobic *Kalanchoe*, *Mesua* and *Litchi* leaf surfaces have shown shorter contact time compared to *Ziziphus* leaf surfaces due to distinct adhesion features.

5.5 Conclusion

- In this work, the four distinctly different plant leaf surfaces namely,*Kalanchoe*, *Ziziphus*, *Mesua*, and *Litchi* were considered for droplet bouncing experiments.
- The *Kalanchoe* and *Ziziphus* leaf surfaces exibit superhydrophobicity with low and high adhesion; respectively. However, *Mesua*, and *Litchi* leaf surfaces posess hydrophobicity with high adhesion features. Following important findings are revealed from CA measurements.
  - (i) *Kalanchoe* leaf surface: WCA ∼ 156° ± 2° CAH ∼ 4°.
  - (ii) *Ziziphus* leaf surface: WCA ∼ 151° ± 2°, CAH ∼ 30°.
  - (iii) *Mesua* leaf surface: WCA ∼ 146° ± 2°, CAH ∼ 39°.
  - (iv) *Litchi* leaf surface: WCA ∼ 130° ± 6°, CAH ∼ 32°.
- The complete rebound of droplet is observed for all leaf surfaces. However, the abaxil *Ziziphus* leaf surface shown partial dynamic wetting transion from Cassie to Wenzel state due to micro-scale porous hairy structure with high adhesion features resulting partial rebound state.
- The droplet's bouncing trajectory, maximum spreading, contact time, and effects of surface inclination were analysed for all leaf specimens.